



Astronomical Test with CMOS on the 60 cm Telescope at the Xinglong Observatory, NAOC

Hai-Yang Mu^{1,2}, Zhou Fan^{1,2}, Yi-Nan Zhu¹, Yu Zhang¹, and Hong Wu^{1,2}

¹ Key Laboratory of Optical Astronomy, National Astronomical Observatories, Chinese Academy of Sciences, Beijing 100101, China; zfan@nao.cas.cn, ynzhu@bao.ac.cn, yzhang@bao.ac.cn, hwyu@bao.ac.cn, hymu@bao.ac.cn

² School of Astronomy and Space Science, University of Chinese Academy of Sciences, Beijing 100049, China

Received 2024 January 30; revised 2024 March 8; accepted 2024 March 12; published 2024 May 2

Abstract

This work shows details of an evaluation of an observational system comprising a complementary metal-oxide-semiconductor detector, 60 cm telescope and filter complement. The system's photometric precision and differential photometric precision, and extinction coefficients were assessed through observations of Supersky flat fields, open clusters, standard stars and exoplanets. Photometry was precision achieved at the 0.02 mag level, with differential photometry of 0.004 mag precision. Extinction was found to agree with previous studies conducted at Xinglong Observatory. Ultimately, the results demonstrate this observing system is capable of precision scientific observations with a charge-coupled device across the optical wavelengths.

Key words: atmospheric effects – instrumentation: detectors – techniques: polarimetric – stars: atmospheres – eclipses

1. Introduction

Since the application of charge-coupled devices (CCDs; Boyle & Smith 1993) to astronomical observation, there has been a significant increase in observation methods. Later with developments in modern semiconductor technology, complementary metal-oxide-semiconductor (CMOS) sensors appeared. However, early CMOS technology was not suitable for scientific astronomical observation due to the high readout noise, and the lower dynamic range compared to CCD technology (Gallaway 2016). Furthermore, the independent readout of each pixel can potentially lead to non-uniformity in the readout levels between pixels. Thus, early CMOS technology was primarily used for non-scientific astronomical imaging.

The advent of scientific CMOS image sensors led to the initial application of CMOS cameras in amateur astronomical observation (Fossum 1997; Bonanno et al. 2003). Advancements in CMOS manufacturing processes have been more and more significant. Currently, only a small difference exists between the readout noise of CMOS devices and CCDs. Further, the dynamic range of CMOS sensors has expanded considerably. In addition, the emergence of back-illuminated CMOS chips has substantially increased quantum efficiency (Bigas et al. 2006; Li et al. 2006). The readout noise of CMOS devices approaches that of CCDs. As a result, the difference between the performance of CCD and CMOS image sensors continues to diminish.

Although CMOS applications are popularly used by amateur astronomers, CCDs are still widely used in professional

astronomical observations. However, CMOS has been employed in some sky survey projects, such as the Argus Optical Array (Law et al. 2022), the Large Array Survey Telescope (Ofek et al. 2023), or the next-generation telescope of the ATLAS project (Tonry et al. 2018), which will be installed at the ATLAS-Teide observatory on Teide mountain (Licandro et al. 2023). Some of them use CMOS because of its low cost and ability of wide field-of-view and high signal-to-noise ratio (SNR) measurements. In fact, there are also differences in performance between different brands of CMOS. A considerable amount of testing has been done on CMOS (Karpov et al. 2020; Qiu et al. 2021; Alarcon et al. 2023), which has revealed the following unique problems such as the salt and pepper noise that are not seen with CCDs. However, these tests are solely on performance, and the astronomical tests of CMOS, such as photometric accuracy and extinction coefficient, are rare.

In this article, we test the CMOS product SONY IMX455 chip, which is back-illuminated. In Section 2, the observation system is introduced. In Section 3, the processing of the data reduction is described. In Section 4, the results and analysis of astronomical observations are introduced. Section 5 presents the summary and conclusions.

2. Observations

2.1. Observation System

The observation system used in this article includes a telescope, CMOS camera and filters.

Table 1
Parameters of the CMOS Camera

Features	Specifications
Sensor	SONY IMX455
Pixel number	9576×6833
Max full frame rate	2 fps
Pixel size	$3.76 \mu\text{m} \times 3.76 \mu\text{m}$
Imaging area	$36 \text{ mm} \times 24 \text{ mm}$
A/D conversion	16 bit
Full well	$51400e^-$
Readout noise	$1.2 \sim 3.5e^-$
Dark current noise	$0.003e^- \text{ s}^{-1} \text{ pix}^{-1}$ at 0°C
Shutter Type	rolling shutter
Fill factor	100%
Operating temperature	Below ambient temperature $30^\circ\text{C} \sim 35^\circ\text{C}$

The telescope used in this observation is the 60 cm telescope at the Xinglong Observatory of National Astronomical Observatories, Chinese Academy of Sciences (NAOC). The telescope has the following parameters from the official observatory website³:

1. Aperture: 60 cm
2. Field of view: $18' \times 18'$
3. Focal ratio of primary mirror: $F/3.28$
4. Corrected focal ratio of primary focus: $F/4.23$

The 60 cm telescope achieved first light in 1964 as a technical test telescope for the 2.16 m telescope at Xinglong Observatory. It was fully commissioned in 1968 after a series of upgrades. Since 1974, the telescope has been used for photometric observations of variable stars such as eclipsing binaries and pulsating stars. From 1995 to 2000 it was used primarily for a supernova search survey. Since 2000 it has been focused on variable star observations.

The IMX455⁴ (Alarcon et al. 2023) is a back-illuminated CMOS sensor, which is installed in the ZWO ASI6200MM PRO camera in this observation system. Table 1 shows some of the parameters of the camera, and detailed information can be referenced at the official website.⁵ We can see that the dark current noise is only $0.003e^- \text{ s}^{-1} \text{ pix}^{-1}$ at 0°C , which means that a 5 minute exposure would result in only $0.9e^-$ dark current noise, which is negligible. Pixel size is $3.76 \mu\text{m}$. Pixel scale is $0''.306 \text{ pixel}^{-1}$ for our testing system.

We used the Johnson-Bessell filter system (Bessell 1990). Only *BVRI* are applied, and their corresponding central wavelengths are shown in the Table 2.ghh

Table 2

Center Wavelengths Corresponding to *BVRI* in Johnson-Bessell filter system

$\lambda_c(\text{nm})$	<i>B</i>	<i>V</i>	<i>R</i>	<i>I</i>
Johnson	440	550	640	806(Bessell)

2.2. Observation

2.2.1. Observation Plan for Tests

In this article, the tests mainly include: Supersky flat field, accuracy of photometry, accuracy of differential photometry and calculation of extinction coefficients during CMOS observations.

2.2.1.1. Supersky Flat Field

The primary goal of capturing a Supersky flat field is to compare it to dusk and dawn flat fields. This comparison allows one to assess differences between dusk and dawn sky illumination patterns. A Supersky flat field is obtained by observing low stellar density fields. A fixed exposure time was adopted, with the telescope being offset slightly between individual exposures, yielding approximately 300 images acquired across three bands.

2.2.1.2. Open Clusters

To measure the photometric accuracy, we observed four open clusters, NGC 6913, NGC 7243, NGC 6811 and NGC 744, with consideration for time constraints on individual exposures. Open clusters were selected based on having an optimal density of stars within the field-of-view to balance sufficient numbers with avoiding excessive crowding. Additionally, open clusters contain a large population of variable stars and binary systems, as noted by Abazajian et al. (2009). These unique features of open clusters informed our choice to utilize them in our calculations. Table 3 lists the specific targets of the photographed open clusters in our observing program. Open clusters serve as ideal targets to test photometric accuracy through calibration to literature values.

2.2.1.3. Standard Stars

The extinction coefficients were computed from observations of standard stars. The method involves monitoring standard stars throughout the whole night from rise to set. Photometric standard stars have precisely determined flux measurements across various photometric systems (Oke & Gunn 1983; Landolt 2007a, 2013). Through measurements using a CCD camera or photometer, the brightness or flux of another object can be determined by comparison to the standards. By tracking standard star magnitudes versus airmass, the extinction coefficient was derived. In this work, standard

³ Reference Site: <http://www.xinglong-naoc.cn/html/gcyq/60/detail-28.html>.

⁴ Reference Site: https://www.sony-semicon.com/files/62/pdf/p-13-IMX455AQK_BQK_ALK_Flyer.pdf.

⁵ Reference Site: https://i.cmoscool.com/zwo-website/manuals/ASI6200MM%20Pro_Manual_CN_V1.0.pdf.

Table 3
Information on the Observed Objects

Name	R.A. (J2000)	Decl. (J2000)	Vmag	Deep	Duration/minutes	Type	Purpose
NGC 6913	01 50 41.71	+21 45 35.89	6.6	Open cluster	photometric accuracy
NGC 7243	22 15 9.12	+49 49 48.00	6.4	Open cluster	photometric accuracy
NGC 6811	19 37 21.60	+46 22 40.80	7.74	Open cluster	photometric accuracy
NGC 744	01 58 36.480	+55 28 22.80	8.38	Open cluster	photometric accuracy
SA 20-43	00 45 42.45	+45 35 15.43	10.4	Standard star	extinction coefficient
BD+39 3312	18 04 28	+39 40 38	9.78	Standard star	extinction coefficients
HAT-P-32 b	02 04 10.24	+46 41 16.8	11.29	0.0244	186.5	Exoplanet	differential photometric accuracy
WASP-33 b	02 26 51.08	+37 33 02.5	8.3	0.0151	163	Exoplanet	differential photometric accuracy

stars were from Landolt's catalog (Landolt 2007b, 2013). Table 3 lists the standard stars selected for our observations.

2.2.1.4. Exoplanet

To measure the differential photometric precision, we observe two exoplanets. Table 3 lists the two observed targets: HAT-P-32 b and WASP-33 b. The approach involved capturing single-band *V* exposure frames during the transit. Both targets were monitored continuously from one hour before until one hour after the transit event of the exoplanet.

2.2.2. Observation

Due to the limit imposed by mechanical tracking for the 60 cm telescope, the maximum observation time for a single target is 30 s. For the camera settings, the GAIN parameter is set to 100 which refers to the gain value of $0.25e^-/\text{ADU}$, and the readout noise value is $1.5e^-$. The camera was cooled to -10°C .

Our observation log is listed in Table 4. The relevant information includes: Primary Observation Targets, Observational time, Band, Exposure and Frame. Our main observation period is from 2022 September 23 through September 30. Prior to each night, the imaging quality was assessed and the optical focus adjusted to optimize image quality. Each open cluster was observed sequentially in four filters, with 80 images per band. Standard stars were monitored throughout entire nights in all four filters. Exoplanet targets were observed in *V* band alone for the whole night. The observation strategy employed is different between different targets: HAT-P-32 b was in normal focus, while WASP-33 b was defocused.

Table 4
The Observation Log Table, Listing Primary Observation Targets, Observational Time, Band, Exposure and Frame

Primary Observation Targets	Observational Time (YYYY/MM/DD)	Band	Exposure Time (s)	Frame
NGC 6913	2022/09/24	<i>B</i>	5	80
		<i>V</i>	5	80
		<i>R</i>	5	80
		<i>I</i>	5	80
NGC 7243	2022/09/24	<i>B</i>	5	80
		<i>V</i>	5	80
		<i>R</i>	5	80
		<i>I</i>	5	80
HAT-P-32 b	2022/09/26	<i>V</i>	30	541
WASP-33 b	2022/09/27	<i>V</i>	20	548
SA 20-43	2022/09/28	<i>B</i>	20	282
		<i>V</i>	20	282
		<i>R</i>	10	282
		<i>I</i>	20	282
Supersky flat field	2022/09/29	<i>B</i>	20	100
		<i>V</i>	20	284
		<i>R</i>	20	100
NGC 6811	2022/09/30	<i>B</i>	30	80
		<i>V</i>	30	80
		<i>R</i>	15	80
		<i>I</i>	15	80
NGC 744	2022/09/30	<i>B</i>	25	80
		<i>V</i>	25	80
		<i>R</i>	25	80
		<i>I</i>	25	80
BD+39 3312	2023/06/21	<i>B</i>	4	532
		<i>V</i>	4	532
		<i>R</i>	4	532
		<i>I</i>	16	532

3. Data Reduction

3.1. Image Trimming

As described in Section 2, the approximate field-of-view of the 60 cm telescope is $18' \times 18'$. However, during observations it was found that the full field captured by the camera subtended roughly $32' \times 48'$. Therefore, trimming of the images was required to extract the relevant field-of-view for

analysis. To obtain the best illuminated field from the telescope, only a subsection of the full CMOS frame corresponding to the area illuminated by the telescope optics was retained for photometry.

After the trimming, the image data size is changed to $3354 \times 3354 \text{ pixel}^2$, and its field of view is changed to

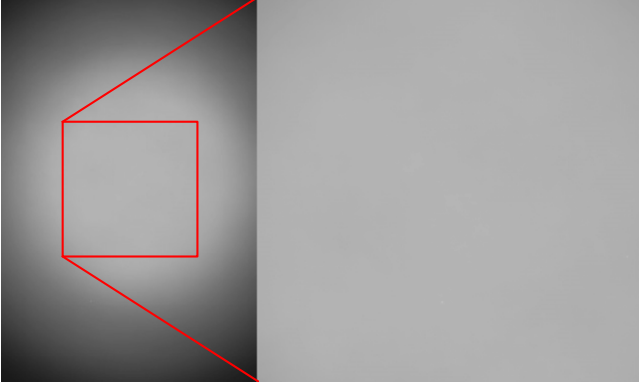


Figure 1. Image data trim; the right panel is before trim, the left panel is after trim.

$17'05 \times 17'05$. The pre-trimmed and post-trimmed planar fields are shown in Figure 1, where the left is the pre-trimmed planar field, and the box in the figure is the trimmed range. The right panel is the trimmed flat field. All bias frames, flat fields and science target images were trimmed for further processing and analysis.

3.2. Bias

This section aims to evaluate the stability of CMOS bias frames and investigate any temporal variations before and after observation with CMOS. Bias images were taken at dusk and dawn on different nights. Examination of the biases indicates the background stabilizes at approximately 510 ADU. First we combined bias frames using median. The median value was retained to mitigate the effects of salt and pepper noise (Alarcon et al. 2023). Differences between biases were analyzed to highlight any temporal variations. Table 5(a) shows the differences between the mean of the combined dusk bias and the combined dawn bias each day. Table 5(b) shows the differences between the mean of the 24th combined dusk and the other day's combined dusk biases.

These comparisons demonstrate the bias stability over the whole observation nights. Thus, we conclude the CMOS detector operation was stable throughout the observation period. During pre-processing, the dusk bias frame was subtracted from both the raw science images and flat fields at each night. Overall, the characterized bias stability supports reuse of a single master bias constructed from dusk frames only, without need to consider time-variable corrections over the observation run.

3.3. Flat Field

Flat field is essential for processing observational data not only to correct for the unevenness of the illumination sky, but

Table 5

Bias Comparison, the Difference Value is the Numerical Difference between the Highest Peak and the Lowest Valley in the Resulting Image Post the Subtraction of the Two Bias Images

(a) Dawn Bias versus Dusk Bias, Dusk Bias Subtracting Dawn Bias	
Date (YYYYMMDD)	Difference Value (ADU)
20220924	-0.09
20220925	-0.048
20220926	-0.072
20220927	-0.054
20220928	-0.074
20220929	-0.007

(b) With 24 Dusk Biases, Others days' Dusk Bias Subtracting 24 Dusk Biases

Date (YYYYMMDD)	Difference Value (ADU)
20220925	0.02
20220926	0.044
20220927	0.044
20220928	0.063
20220929	0.045

Table 6

Flat Comparison Table for Different Dusk and Dawn Dates

Date (YYYYMMDD)/Filter	<i>B</i> (%)	<i>V</i> (%)	<i>R</i> (%)	<i>I</i> (%)
20220924	0.5	0.4	0.4	0.9
20220925	0.5	0.4	0.3	1.2
20220926	0.2	0.3	0.1	1.4
20220927	0.3	0.3	0.7	1.5
20220928	0.4	0.5	0.6	1.7
20220929	0.9	0.9	0.9	UNOBSERVED

Note. The table's filter presents the comparison result of each band, which is the result of the difference in the peak-to-valley value after dividing the two smoothed images.

also to correct differences between the amplifiers for each pixel.

Table 6 presents the outcomes of calculating the ratio of the median combined flat field captured during dusk versus that obtained during dawn for each day. This ratio represents the variation between the maximum and minimum of the images of the two flat fields after normalizing, and smoothing via the median filter. This metric provides a measurement of the illumination uniformity achieved across each band flat. Comparing the values among the different dusk and dawn flats indicates any variation introduced by changing illumination conditions at dusk versus dawn. Table 6 provides a comparison within each band, revealing that the median difference is within 1% in the *B*, *V* and *R* bands, and within 2% in the *I* band.

Table 7 presents results from dividing the median value of the dusk flat field for each night during September 24–29.

Table 7
The Rest of the Days and 24 Dusk Flat Comparison Table

Date (YYYYMMDD)/Filter	<i>B</i> (%)	<i>V</i> (%)	<i>R</i> (%)	<i>I</i> (%)
20220925	0.8	0.4	0.5	0.3
20220926	0.6	0.3	0.5	0.3
20220927	0.7	0.6	0.4	0.4
20220928	0.6	0.5	0.6	0.3
20220929	0.6	0.8	0.7	UNOBSERVED

Note. The table's filter presents the comparison result of each band, which is the result of the difference in the peak-to-valley value from dividing the two smoothed images.

These values indicate the level of consistency between daily flats during the observation period. As expected, flat fields agree to within 1% in all bands. This consistency validates the combined master flat field better to than 1%, but at this level it will not significantly impact science photometry. The temporal stability of the flats supports their use for corrections throughout the observation window without introducing spurious variations.

Therefore, we took the image that had the bias correction and dusk flat field correction to obtain the scientific images.

3.4. Photometry

We used Source-Extractor (SExtractor) tools for photometric measurements. SExtractor's automatic aperture photometry routine is derived from Kron's "first moment" algorithm (Kron 1980). For details, see SExtractor's manual (Bertin & Arnouts 1996).⁶ In Table 8, we present some parameters of SExtractor. DETECT_THRESH represents the threshold for star detection, for which we have opted for the default value. PHOT_AUTOPARAMS denotes the parameters for automatic aperture photometry, for which we have also chosen the default settings. Additionally, BACKPHOTO_TYPE specifies the background calculation method, with our selection being LOCAL to compute the flux error using local background estimation. The formula used by SExtractor to calculate the flux error is as follows

$$\text{Fluxerr} = \sqrt{\sum_{i \in A} \left(\sigma_i^2 + \frac{p_i}{g_i} \right)}. \quad (1)$$

Equation (1): where A is the set of pixels defining the photometric aperture, σ_i the standard deviation (std) of noise (in ADU) estimated from the local background, p_i the measurement image pixel value subtracted from the background and g_i the effective detector gain in e/ADU at pixel i . Note that this

Table 8
SExtractor Parameters

Parameter	Specifications
DETECT_MINAREA	50
DETECT_THRESH	1.5
PHOT_AUTOPARAMS	2.5, 3.5
SATUR_LEVEL	65 525.0
MAG_ZEROPOINT	25
GAIN	0.25
PIXEL_SCALE	0.306
BACKPHOTO_TYPE	LOCAL

error estimate provides a lower limit of the true uncertainty, as it only takes into account photon and detector noise.

With aperture photometry and target extraction we can obtain the light curve of the target (Huang et al. 2022). However, before we do this, we need to correct the exposure time. We need to correct the exposure time t and magnitude m_{phot} obtained from the photometry, to determine the ultimate instrumental magnitude

$$m_{\text{inst}} = m_{\text{phot}} + 2.5 \log_{10}(t). \quad (2)$$

3.5. System Conversion

After the exposure time correction, we carry out the calibration and filter system correction. We introduce the reference catalog—Gaia's synthetic photometry (Gaia-SP; Gaia Collaboration et al. 2023) and Gaia Data Release 3 (DR3) (Gaia Collaboration et al. 2023). Here we applied Equation (3), to make corrections and, according to different situations to transform the formula, to simplify the process

$$\begin{aligned} m_{B,\text{inst}} &= m_{B,\text{Gaia-sp}} + c_B + k_{1,B} \cdot X \\ &\quad + k_{2,B} \cdot (m_{B,\text{Gaia-sp}} - m_{V,\text{Gaia-sp}}) \\ m_{V,\text{inst}} &= m_{V,\text{Gaia-sp}} + c_V + k_{1,V} \cdot X \\ &\quad + k_{2,V} \cdot (m_{B,\text{Gaia-sp}} - m_{V,\text{Gaia-sp}}) \\ m_{R,\text{inst}} &= m_{R,\text{Gaia-sp}} + c_R + k_{1,R} \cdot X \\ &\quad + k_{2,R} \cdot (m_{V,\text{Gaia-sp}} - m_{R,\text{Gaia-sp}}) \\ m_{I,\text{inst}} &= m_{I,\text{Gaia-sp}} + c_I + k_{1,I} \cdot X \\ &\quad + k_{2,I} \cdot (m_{V,\text{Gaia-sp}} - m_{I,\text{Gaia-sp}}) \end{aligned} \quad (3)$$

Here m_{inst} is the instrumental magnitude, $m_{\text{Gaia-sp}}$ is the magnitude with reference to the Gaia-SP (Gaia Collaboration et al. 2023) catalog, X is airmass, k_1 is the extinction coefficient corresponding to a certain band, k_2 is the color coefficient corresponding to the two systems and C is the zero-point between the two systems.

Flux calibrations are usually calibrated using the field star maps that are photographed and processed. The magnitude

⁶ Reference Site: <https://sextractor.readthedocs.io/en/latest/Introduction.html>.

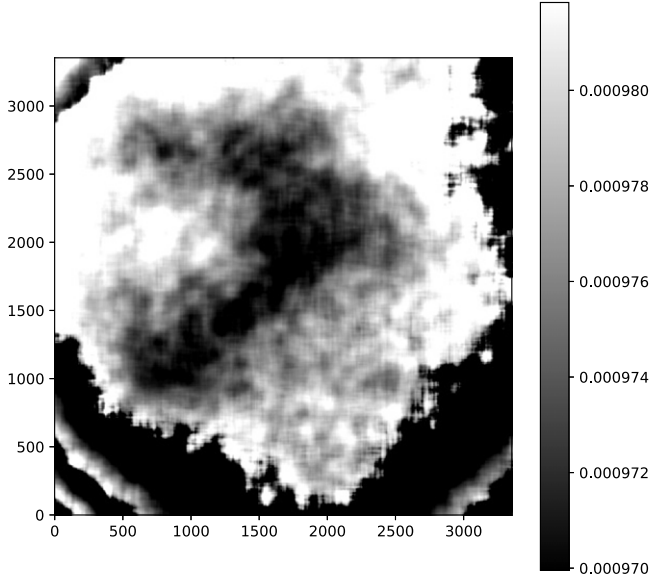


Figure 2. This image is the division of the Supersky flat field and the dusk and dawn flat field, and then the image is smoothed with a box size of 100 pixel.

calibrations used here are those that convert the instrumental magnitude to the true magnitude, and here we use the Vega system. Because of the high accuracy Gaia DR3 data, we have selected Gaia DR3 as the reference magnitude.

4. Results and Analysis

4.1. Supersky Flat Field

This comparison evaluates the illumination differences between the Supersky flat field and flat field from dusk and dawn. The comparison reveals discrepancies in the sky background. Figure 2 displays the image after dividing the Supersky flat field and the dusk and dawn flat field, followed by smoothing the image to a size of 100. Table 9(a) is obtained by calculating the difference in terms of the peak-to-valley value in this figure. It presents results comparing the Supersky flat to dawn flats, using the same methodology for analysis. As flat fields were only obtained in three bands, comparisons are shown for those bands. The differences between dawn flats on each night are within one percent, matching expectations. Similarly, Table 9(b) compares the Supersky flat to dusk flats, also showing percent level agreement with the dusk reference each night. All flat fields show sub-percent level consistency. The Supersky flat field is used as an independent check of the dusk and dawn flat field's ability to represent the illumination.

Table 9 demonstrates that the flat field is stable at slightly under 0.01 during nights. Furthermore, each band flat field and the Supersky flat field remain within 1% over the entire observation period. This is in contrast to the Supersky flat field

Table 9
Supersky and Different Day Flat Comparison

(a) Supersky and Different Dawn Flat Comparison			
Date(YYYYMMDD)/Filter	B (%)	V (%)	R (%)
20220924	0.3	0.3	0.4
20220925	0.7	0.8	0.8
20220926	0.4	0.4	0.5
20220927	0.4	0.3	0.4
20220928	0.4	0.4	0.4
20220929	0.4	0.4	0.4

(b) Supersky and Different Dusk Flat Comparison			
Date(YYYYMMDD)/Filter	B (%)	V (%)	R (%)
20220924	0.4	0.6	0.7
20220925	0.4	0.5	0.6
20220926	0.5	0.5	0.5
20220927	0.4	0.4	0.6
20220928	0.3	0.3	0.3
20220929	0.6	0.7	0.9

Table 10
Limiting Magnitudes at 3σ and 5σ for Each Band

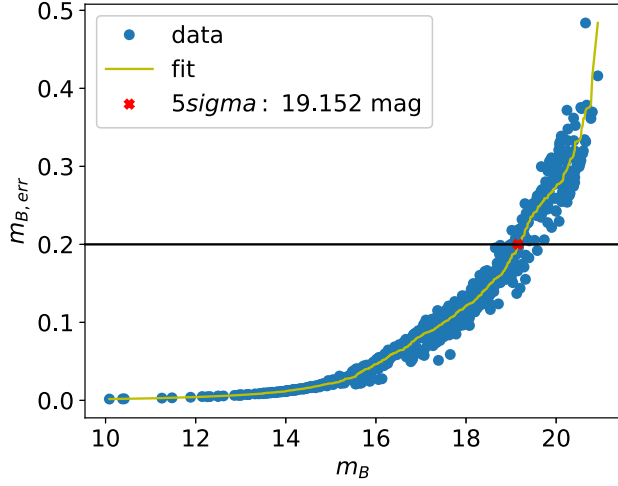
Filter	5σ (mag)	Accuracy of Fitting	Exposure Time (s)
B	19.152	0.042	30
V	19.205	0.043	30
R	18.747	0.053	30
I	17.361	0.052	30

for the 60 cm observation field. It suggests that changes in observing conditions like airmass or twilight illumination are less than 0.01, as validated by the independent Supersky flat.

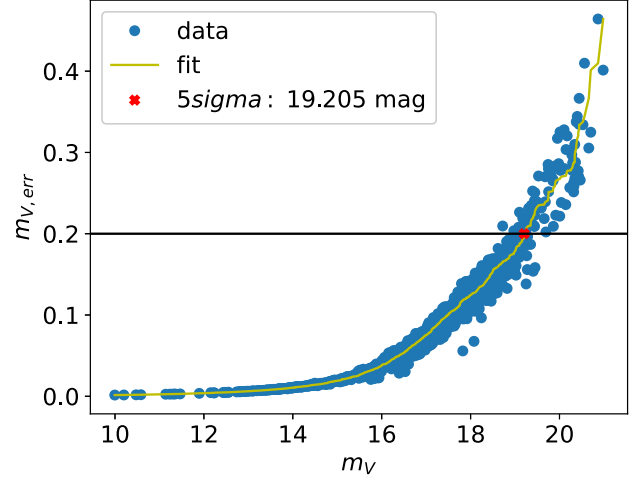
4.2. Limiting Magnitude

The limiting magnitude is an important indicator of an observing system, demonstrating the observing system's capability. In this system, due to the mechanical limitations of the telescope, we can only use a single exposure up to 30 s. Below are the limiting magnitudes calculated by the open clusters, after calibrating and calculating the limiting magnitudes in the *BVRI* bands and at 3σ and 5σ . Figure 3 displays the magnitude-error plots and magnitude statistics after the calibration. Here the m_{err} is obtained from Equation (1).

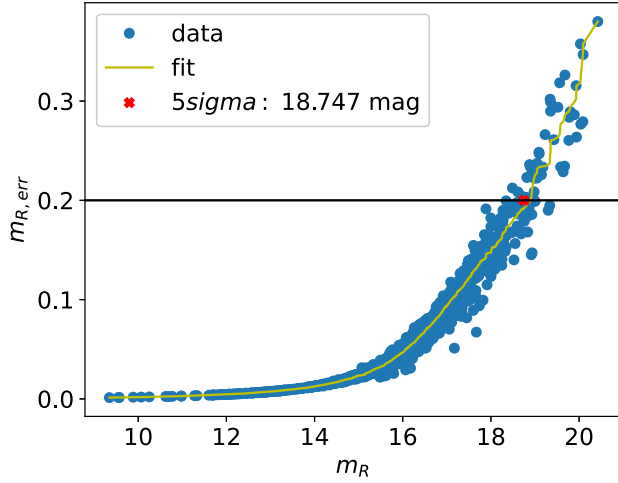
From Table 10 we see that limiting magnitude variation in different bands corresponds to the quantum efficiency of the CMOS, and the limiting magnitude at 5σ in the V band is 19.205 mag, as expected.



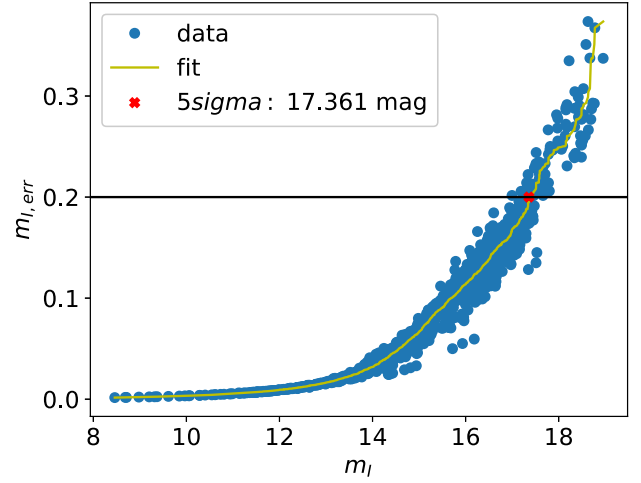
(a) B-band magnitude-error plot



(b) V-band magnitude-error plot



(c) R-band magnitude-error plot



(d) I-band magnitude-error plot

Figure 3. The 5σ SNR limiting magnitude of each band at 30 s exposures. The calibrated magnitude is on the x-axis and magnitude error on the y-axis. The blue data points represent the observed data, the yellow curve is a fitted curve to the magnitude error and the red markers are points with an SNR of 5σ . The plot shows that the limiting magnitude is 19.152 mag in B-band, 19.205 mag in V-band, 18.747 mag in R-band and 17.361 mag in I-band.

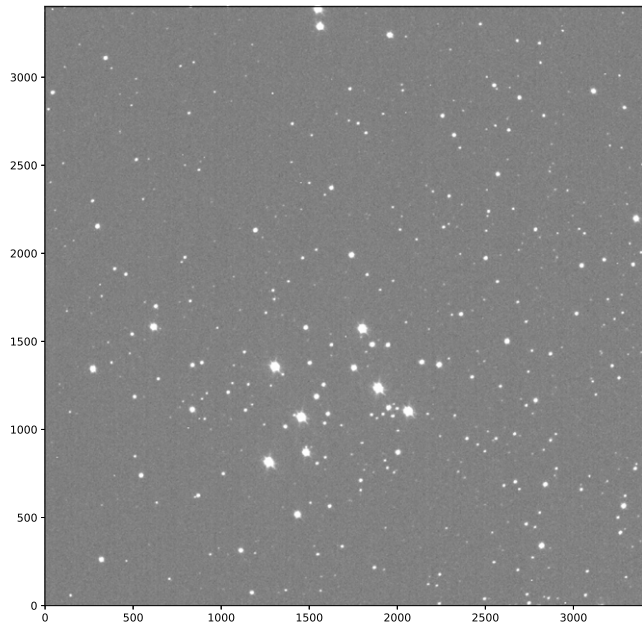
4.3. Open Clusters

Table 3 shows four open star clusters that we observed, namely NGC 6913, NGC 7243, NGC 6811 and NGC 744. Figure 4 displays their R-band trimming images. In this section, we will separately introduce the imaging and processing results of each open star cluster.

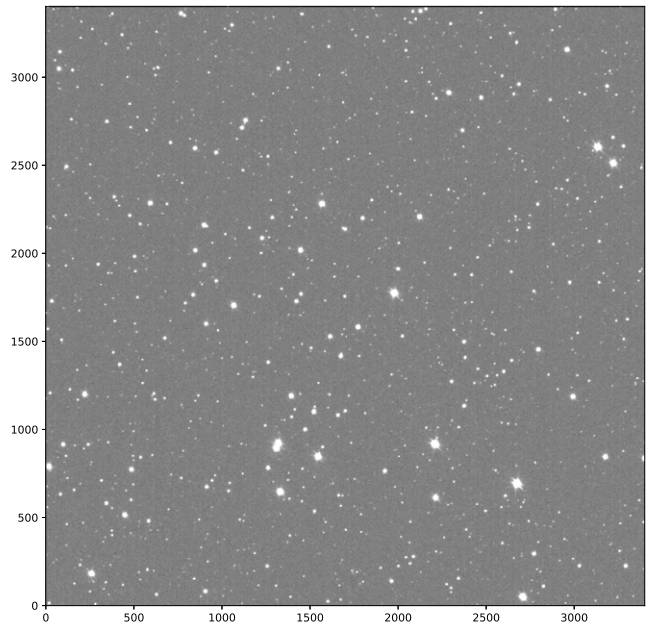
After completing the photometry, the reference magnitude we used was Gaia-SP. Based on the characteristics of open clusters, since in the same field, the extinction between the individual stars can be almost equal, we regard $k_1 \times X$ as a

constant, and thus Equation (3) becomes:

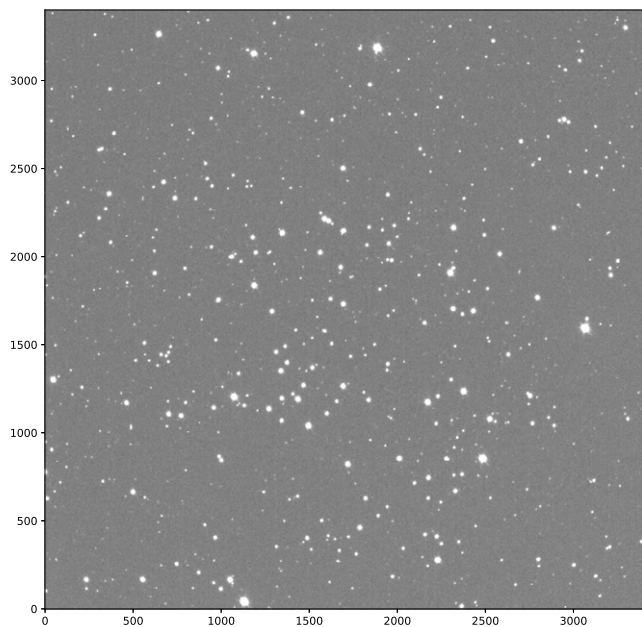
$$\begin{aligned}
 m_{B,\text{inst}} &= m_{B,\text{Gaia-sp}} + c_B + \text{constant} \\
 &\quad + k_{2,B} \cdot (m_{B,\text{Gaia-sp}} - m_{V,\text{Gaia-sp}}) \\
 m_{V,\text{inst}} &= m_{V,\text{Gaia-sp}} + c_V + \text{constant} \\
 &\quad + k_{2,V} \cdot (m_{B,\text{Gaia-sp}} - m_{V,\text{Gaia-sp}}) \\
 m_{R,\text{inst}} &= m_{R,\text{Gaia-sp}} + c_R + \text{constant} \\
 &\quad + k_{2,R} \cdot (m_{V,\text{Gaia-sp}} - m_{R,\text{Gaia-sp}}) \\
 m_{I,\text{inst}} &= m_{I,\text{Gaia-sp}} + c_I + \text{constant} \\
 &\quad + k_{2,I} \cdot (m_{V,\text{Gaia-sp}} - m_{I,\text{Gaia-sp}})
 \end{aligned} \tag{4}$$



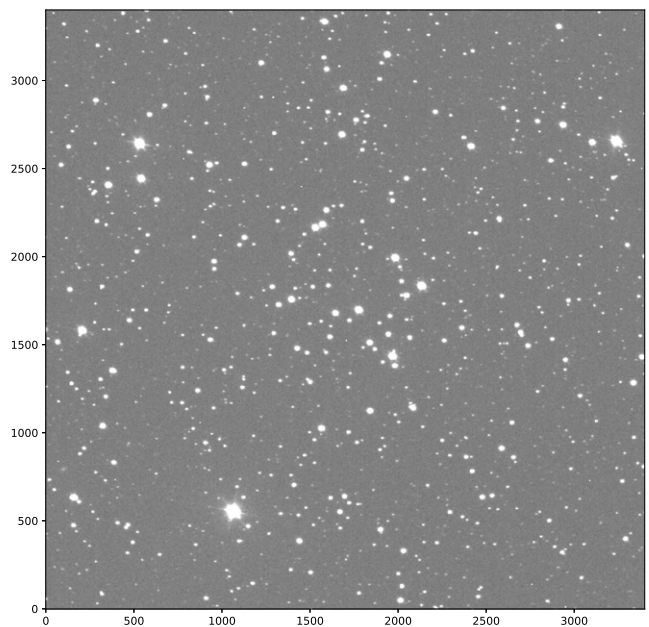
(a) NGC6913 *R*-band



(b) NGC7243 *R*-band



(c) NGC6811 *R*-band



(d) NGC744 *R*-band

Figure 4. *R*-band images of each open cluster.

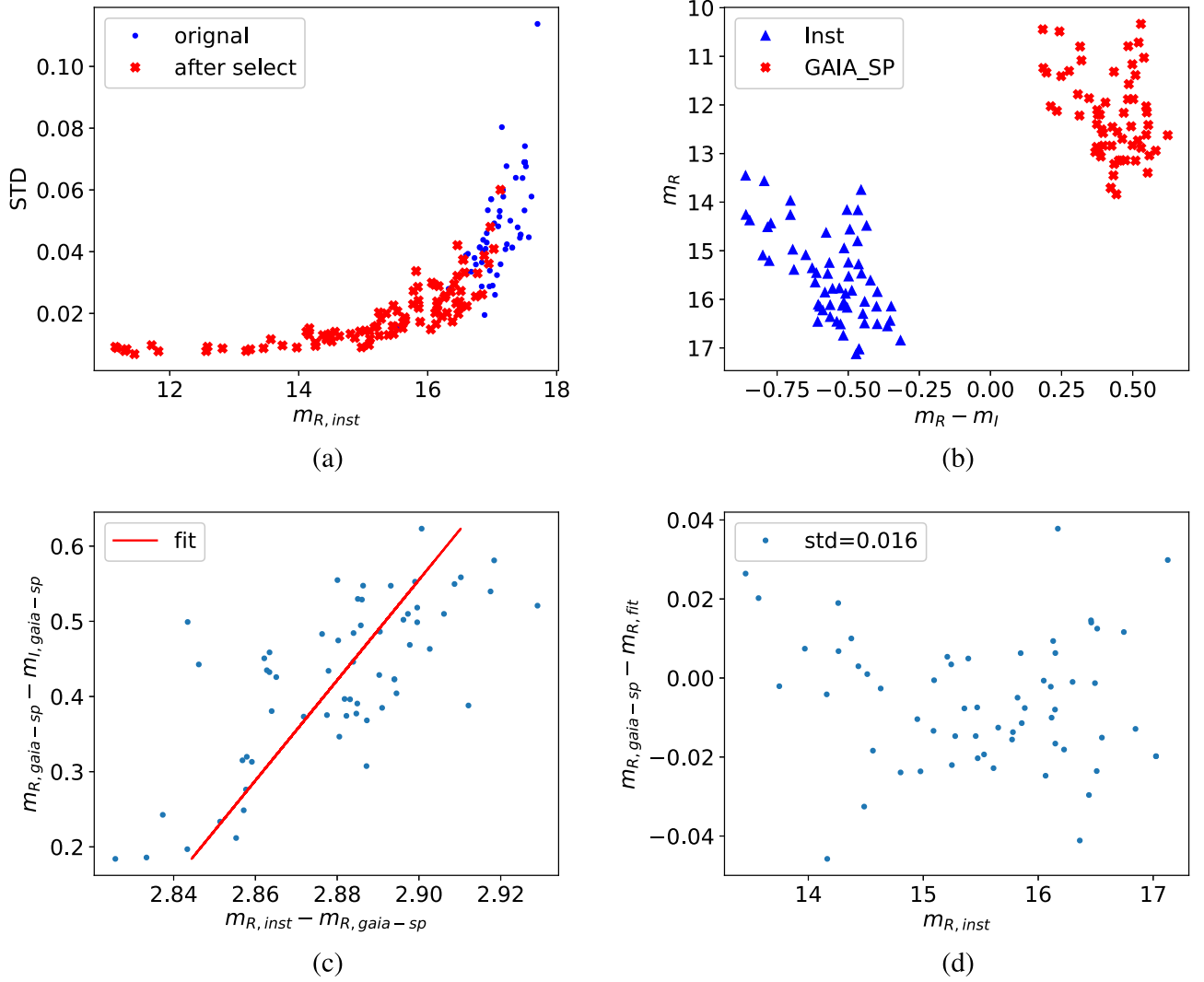


Figure 5. NGC 6913 *R*-band results. (a): The NGC 6913 *R*-band's magnitude-std diagram, with red crosses representing the selected data points and blue dots signifying the excluded data points. (b): NGC 6913 *R*-band's color-magnitude diagram, where the blue triangles represent the instrumental magnitude and red squares correspond to the Gaia-SP magnitude. The horizontal axis is $m_R - m_I$ and the vertical axis is m_R . (c): NGC 6913 *R*-band's magnitude-color diagram, with blue dots representing data points and a red line delineating the fitted line. The horizontal axis of the plot represents the difference between instrumental magnitude and Gaia-SP magnitude, while the vertical axis means Gaia-SP's color, denoted as $m_{R,Gaia-SP} - m_{I,Gaia-SP}$, as described in Equation (4). (d): NGC 6913 *R*-band's magnitude-error diagram, with blue dots representing data points. The horizontal axis represents instrumental magnitude, while the vertical axis means the difference between instrumental magnitude and the fit magnitude according to Equation (4).

We can see that Equation (4) has only two variables, $C + \text{constant}$ and k_2 , from which we can obtain their respective corresponding parameters by simple straight line fitting. The color corrections are combined using Equation (4) (Cousins & Caldwell 2001; Calamida et al. 2018).

4.3.1. NGC 6913

We performed photometry on 80 frames in the same band, and calculated the std of the magnitude distribution for each star over these 80 frame, as depicted in Figure 5(a). It displays the error of stars before our selection, with instrumental

magnitude on the x -axis and the std of the magnitude distribution for each source across the 80 frames on the y -axis. Based on Figure 5(a), we obtained an internal precision of magnitude measurement. We then used Figure 5(a) for target selection, removing the variable stars, saturated stars and non-Zero Age Main-Sequence cases. Finally, we selected member stars and matched the final selected sources to the Gaia-SP star catalog, as depicted in Figure 5(a).

Figure 5(b) compares the color-magnitude plot of the instrumental magnitude with the color-magnitude plot of Gaia-SP. The horizontal axis is the $R-I$ color, and the vertical axis is the R -band magnitude. Figure 5(c) is from Equation (4).

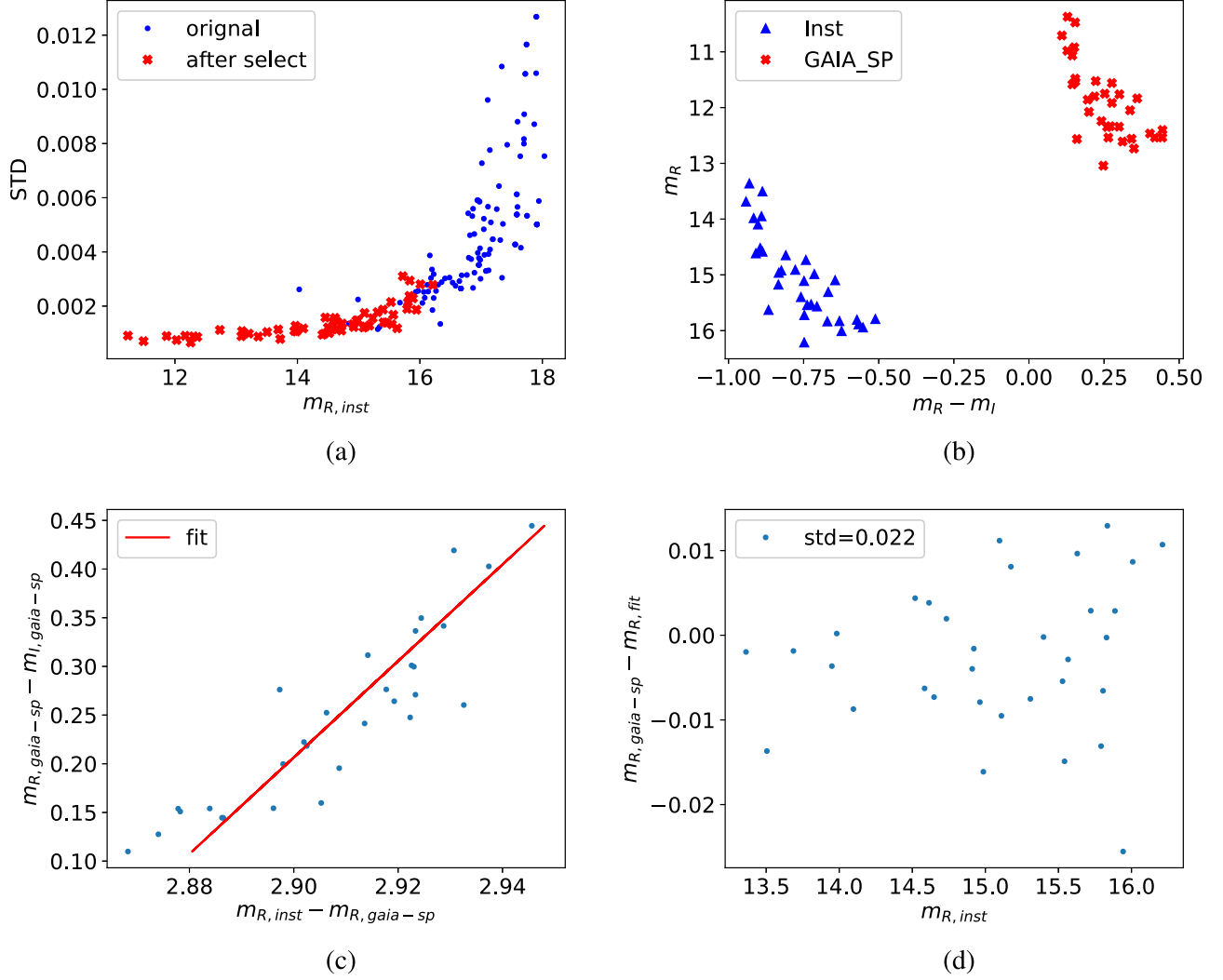


Figure 6. Same as in Figure 5 but for NGC 7243 R -band results. (a): The R -band's magnitude-std diagram, with red crosses representing the selected data points and blue dots signifying the excluded data points. (b): The R -band's color-magnitude diagram, where the blue triangles represent the instrumental magnitude and the red squares are the Gaia-SP magnitude. The horizontal axis is $m_R - m_I$ and the vertical axis is m_R . (c): The R -band's magnitude-color diagram, with blue dots representing data points and a red line delineating the fitted line. The horizontal axis of the plot represents the difference between instrumental magnitude and Gaia-SP magnitude, while the vertical axis means Gaia-SP's color, denoted as $m_{R,Gaia-SP} - m_{I,Gaia-SP}$, as described in Equation (4). (d): The R -band's magnitude-error diagram, with blue dots representing data points. The horizontal axis represents instrumental magnitude, while the vertical axis means the difference between instrumental magnitude and the fitted magnitude according to Equation (4).

The vertical axis in Figure 5(d) is the difference between the corrected magnitude $m_{R,fit}$ and Gaia-SP $m_{Gaia-sp}$. After the final fit, we calculate the difference between the magnitude and Gaia-SP color by multiplying the color coefficient with the color value. The R -band instrumental magnitude is the horizontal axis, and the accuracy obtained from the final photometry is reflected in the std of the label in Figure 5(d). Table 11 displays the coefficients $k_{2,R}$, zeros $c_{R,0} + \text{constant}$

Table 11
The Results about the Observed Open Cluster, $k_{2,R}$ and $c_{0,R} + \text{constant}$ Corresponding to the Parameters of Equation (4)

ID	$k_{2,R}$	$c_{R,0} + \text{constant}$	σ
NGC 6913	0.208	2.789	0.016
NGC 7243	0.168	2.864	0.022
NGC 6811	0.149	2.734	0.011
NGC 744	0.208	2.682	0.019

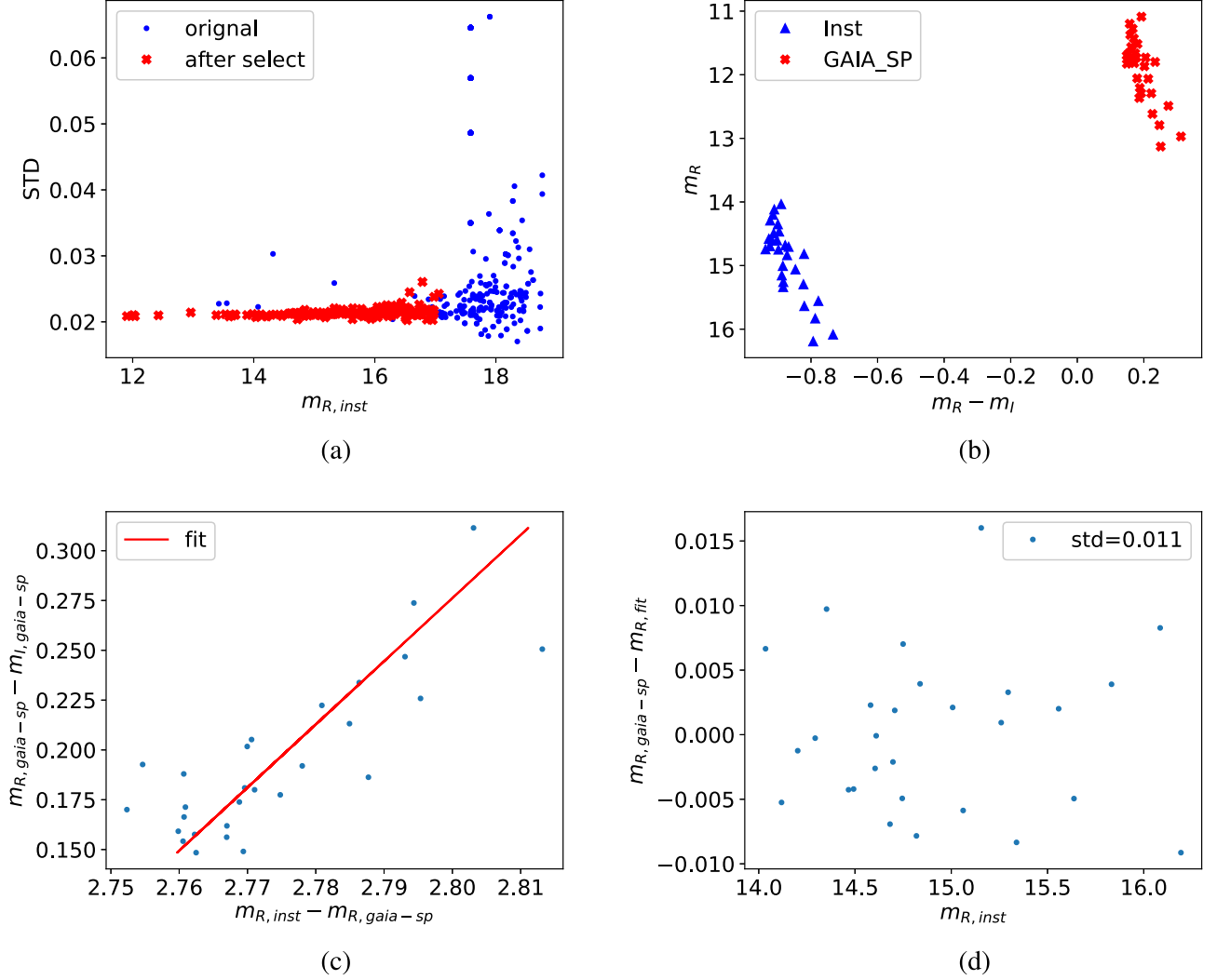


Figure 7. Same as in Figure 5 but for NGC 6811 *R*-band results. (a): The *R*-band's magnitude-std diagram, with red crosses representing the selected data points and blue dots signifying the excluded data points. (b): The *R*-band's color-magnitude diagram, where the blue triangles represent the instrumental magnitude and the red squares are the Gaia-SP magnitude. The horizontal axis is $m_R - m_I$ and the vertical axis is m_R . (c): The *R*-band's magnitude-color diagram, with blue dots representing data points and a red line delineating the fitted line. The horizontal axis of the plot represents the difference between instrumental magnitude and Gaia-SP magnitude, while the vertical axis means Gaia-SP's color, denoted as $m_{R,Gaia-SP} - m_{I,Gaia-SP}$, as described in Equation (4). (d): The *R*-band's magnitude-error diagram, with blue dots marking data points. The horizontal axis represents instrumental magnitude, while the vertical axis means the difference between instrumental magnitude and the fitted magnitude according to Equation (4).

and photometric accuracy that were computed for each open cluster. From this table, we can see that its photometric accuracy is 0.016 mag.

4.3.2. NGC 7243

The processing procedure for NGC 7243 is similar to that of NGC 6913. Figure 6(a) shows the magnitude and std plot obtained with the same processing procedure for NGC 6913.

Finally, by calculating the std of the data in the scatter plot of Figure 6(c), we obtained a photometric accuracy of 0.022 mag.

4.3.3. NGC 6811

The processing procedure for NGC 6811 is similar to that of NGC 6913. Figure 7(a) shows the magnitude and std with the same processing procedure as NGC 6913. Figure 7 also represents the same calculation process as Figure 5 for NGC

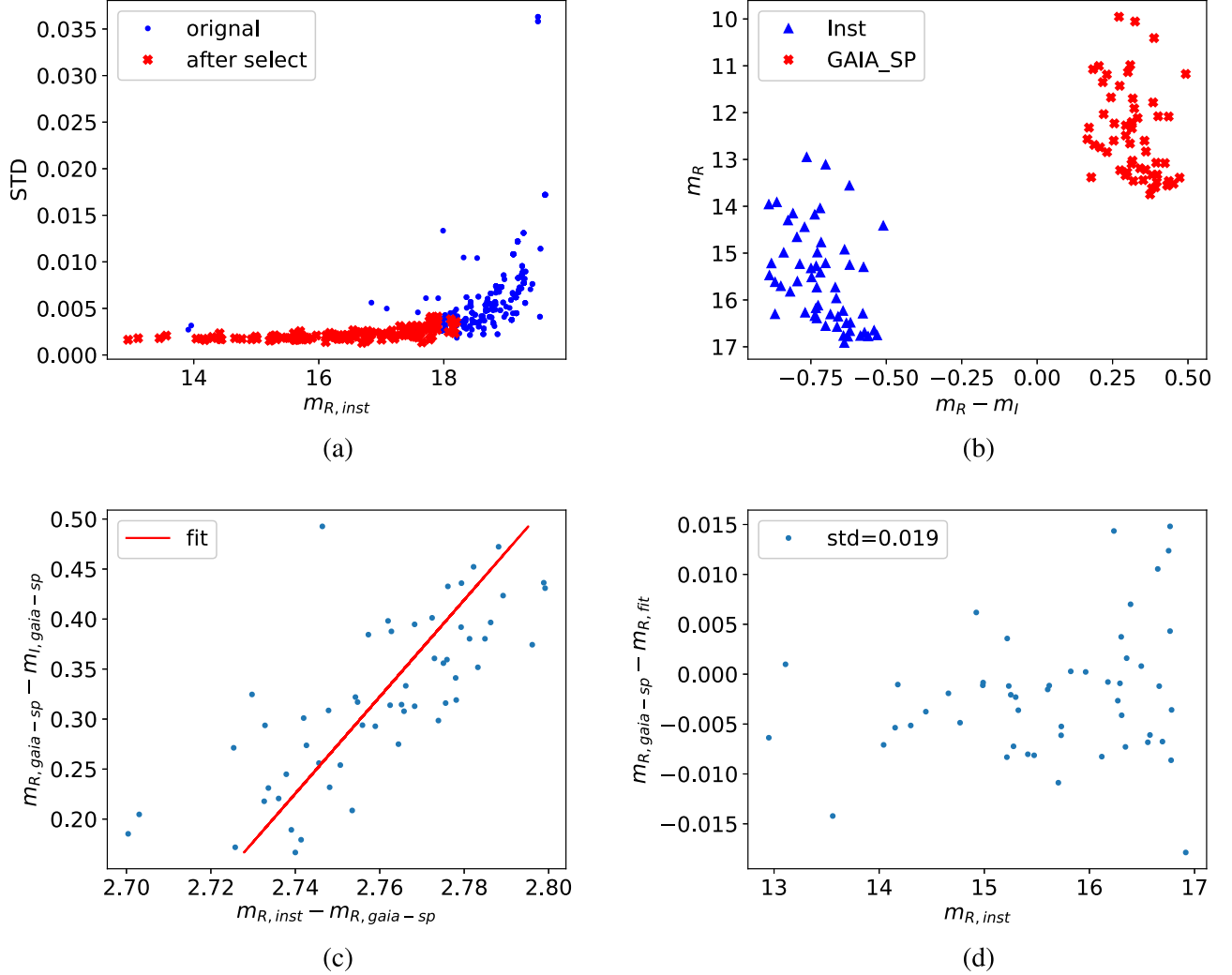


Figure 8. Same as in Figure 5 but for NGC 744 *R*-band results. (a): The *R*-band's magnitude-std diagram, with red crosses representing the selected data points and blue dots signifying the unselected data points. (b): The *R*-band's color-magnitude diagram, where the blue triangles represent the instrumental magnitude and the red squares are the Gaia-SP magnitude. The horizontal axis is $m_R - m_I$ and the vertical axis is m_R . (c): The *R*-band's magnitude-color diagram, with blue dots representing data points and a red line delineating the fitted line. The horizontal axis of the plot represents the difference between instrumental magnitude and Gaia-SP magnitude, while the vertical axis means Gaia-SP's color, denoted as $m_{R,Gaia-SP} - m_{I,Gaia-SP}$, as described in Equation (4). (d): The *R*-band's magnitude-error diagram, with blue dots representing data points. The horizontal axis represents instrumental magnitude, while the vertical axis means the difference between instrumental magnitude and the magnitude obtained by fitting according to Equation (4).

6913. Finally, we calculate the std of the data in the scatter plot of Figure 7(c), with photometric accuracy of 0.011 mag.

4.3.4. NGC 744

The processing procedure for NGC 744 is similar to that of NGC 6913. Figure 8(a) shows the magnitude and std plot obtained through the same processing procedure as NGC 6913. Figure 8 also represents the same calculation process as Figure 5 for NGC 6913. Finally, by calculating the std of the data in the scatter plot of Figure 8(d), we obtained a photometric accuracy of 0.019 mag.

Table 11 summarizes the results for these four open star clusters, where the std listed in the table represents the photometric accuracy. The color coefficient k_2 is not the true system conversion coefficient and incorporates the main order contribution of the cluster. Therefore, the photometric accuracy is approximately 0.02 mag (Landolt 2007a; Munari et al. 2014; Yang et al. 2021).

4.4. Standard Stars

Table 3 shows that we observed two standard stars, namely SA 20-43 and HD 165434, in four different bands. After

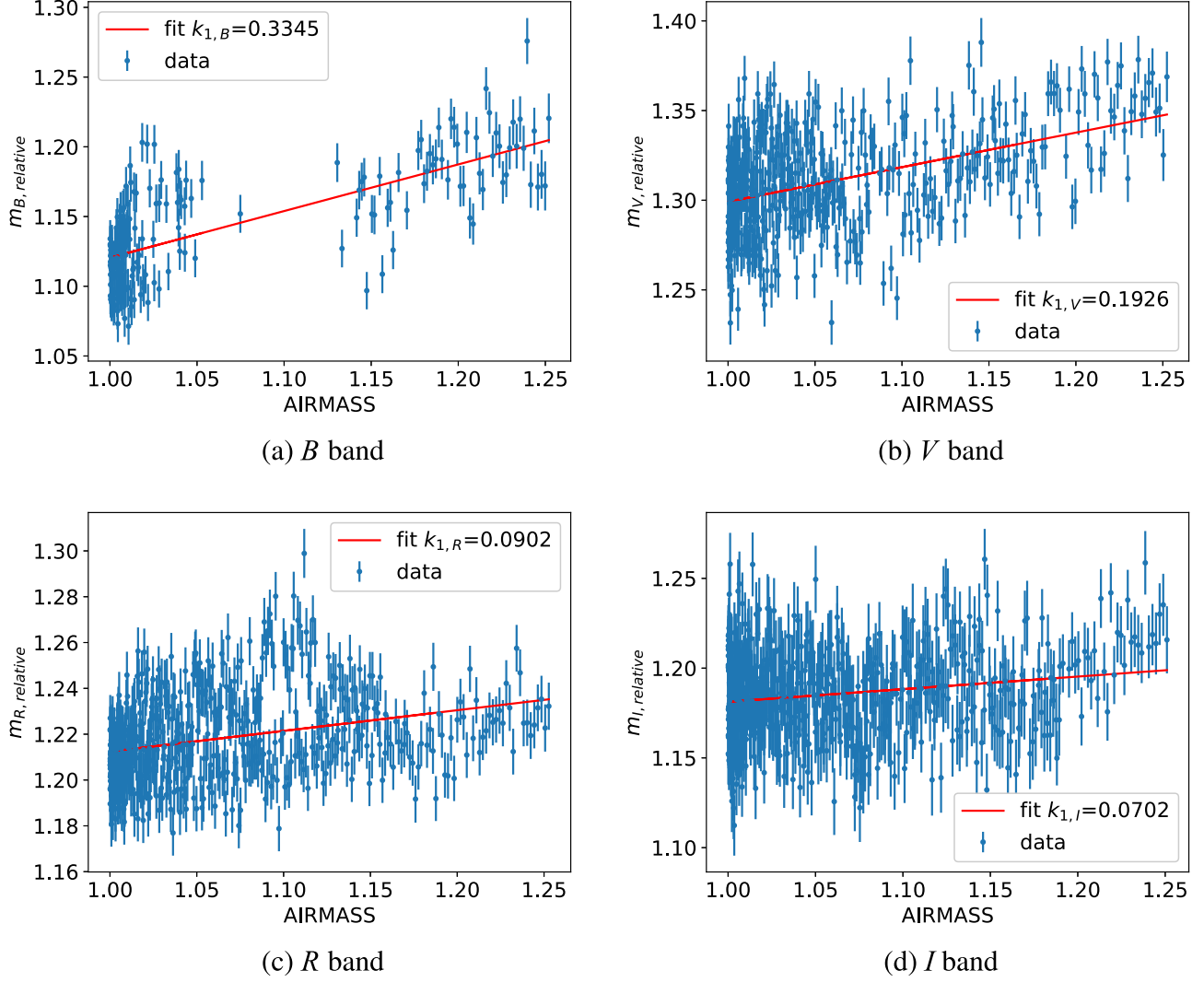


Figure 9. Image of the four bands of BD+39 3312 taken by our observing system. The blue dots represent the observed data, while the red line delineates the fitted line. The x -axis represents airmass, and the y -axis represents the difference between the instrumental magnitude and the Gaia-SP reference magnitude (m_{residual}).

Table 12

The Results of the Four Bands on BD+39 3312 are Obtained by Iterative Correction

	k_1	σ_{k_1}	c_0	σ_{c_0}
<i>B</i>	0.335	0.022	0.786	0.024
<i>V</i>	0.193	0.018	1.107	0.019
<i>R</i>	0.090	0.013	1.122	0.014
<i>I</i>	0.070	0.017	1.011	0.018

completing the pre-processing and photometric processing, we need to extract the light curves of the targets in each band, and then match them with the catalog. After completing these steps, we calculate the extinction coefficients using the system

transformation, Equation (2). At this point, the system transformation formula needs to be modified. Because there is only one target whose color is the same, for this standard star, the color term $k_2 \times (m_{B,\text{Gaia}} - m_{V,\text{Gaia}})$ can be regarded as a constant, and then the formula can be rewritten as:

$$\begin{aligned}
 m_{B,\text{inst}} &= m_{B,\text{Gaia-sp}} + c_B + k_{1,B} \cdot X + \text{constant} \\
 m_{V,\text{inst}} &= m_{V,\text{Gaia-sp}} + c_V + k_{1,V} \cdot X + \text{constant} \\
 m_{R,\text{inst}} &= m_{R,\text{Gaia-sp}} + c_R + k_{1,R} \cdot X + \text{constant} \\
 m_{I,\text{inst}} &= m_{I,\text{Gaia-sp}} + c_I + k_{1,I} \cdot X + \text{constant}
 \end{aligned} \tag{5}$$

We can see that Equation (5) has only two variations, $c + \text{constant}$ and k_1 , from which we obtain their respective corresponding parameters by linear fitting.

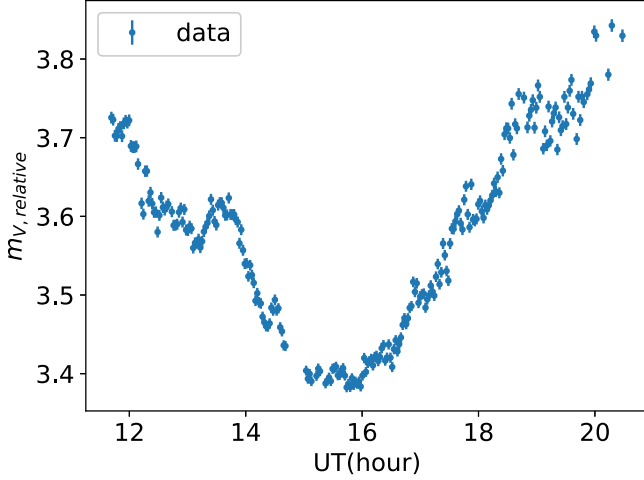


Figure 10. SA 20-43 V-band $m_{\text{residuals}}$ vs. UT.

4.4.1. BD+39 3312

Figure 9 shows the airmass versus magnitude of the standard star BD+39 3312 in each band. The blue dots represent the observed data, while the red line delineates the fitted line. The x -axis represents airmass, and the y -axis means the difference between the instrumental magnitude and the Gaia-SP reference magnitude m_{residual} . Because the observations were made in summer, the range of airmass values shown here is relatively small. Table 12 provides a summary of the fitting results in four bands, with k_1 and c_0 corresponding to the respective coefficients in Equation (5). σ_{k_1} and σ_{c_0} represent the simulated errors. $k_{1,B}$ is 0.335 ± 0.022 , $k_{1,V}$ is 0.193 ± 0.018 , $k_{1,R}$ is 0.090 ± 0.013 and $k_{1,I}$ is 0.070 ± 0.017 .

4.4.2. SA 20-43

Figure 10 shows the variation of the standard star's magnitude with respect to the observation time. The x -axis represents the time in UT (hr), while the y -axis represents the difference between the instrumental magnitude and the Gaia-SP magnitude (m_{residual}). The variation pattern shows a gradual dimming followed by a sudden brightening, continuing to increase in brightness until reaching the maximum. This point indicates the target reaching the zenith. Subsequently, the target undergoes a descending phase with a continuous dimming, followed by a slight brightening and eventually fading. This pattern is observed for all targets within the field of view, indicating the absence of any variability during the observation time. Figure 11 displays the airmass versus magnitude, with the x -axis representing airmass and the y -axis representing the difference between the instrumental magnitude and the Gaia-SP reference magnitude (m_{residual}). The blue triangles represent the ascending phase, while the orange dots signify the descending phase.

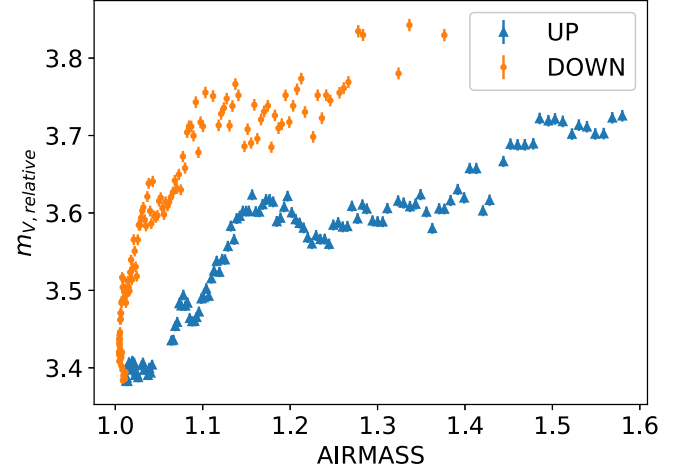


Figure 11. V-band airmass vs. magnitude plot of SA 20-43. Triangles are UP segments, dots are DOWN segments.

This problem has also been discussed in the literature (Yan et al. 2000; Zhou et al. 2001), with two different methods for its correction: One is to correct for the effect of atmospheric extinction by including a band-independent but time-varying zero correction term in its calibration, which was later replaced by a time-varying atmospheric extinction coefficient term (Yan et al. 2000). The other is to use a time-varying atmospheric extinction coefficient term to correct for the effect of atmospheric extinction variations (Zhou et al. 2001). In this work, we used the second method to set up a time-dependent term for the atmospheric extinction coefficient. Since we are only using one target, there is no the color item. To better correct atmospheric extinction, we add a time-varying atmospheric extinction coefficient term. For Equation (5), based on the corrected relationship of the individual standard stars above, this becomes:

$$k'_1 = k_1 + f(\text{UT}). \quad (6)$$

$$f(\text{UT}) = a \cdot \text{UT} + b. \quad (7)$$

$$\begin{aligned} m_{B,\text{inst}} &= m_{B,\text{Gaia-sp}} + c_B \\ &\quad + (k_{1,B} + a_B \cdot \text{UT} + b_B) \cdot X + \text{constant} \\ m_{V,\text{inst}} &= m_{V,\text{Gaia-sp}} + c_V \\ &\quad + (k_{1,V} + a_V \cdot \text{UT} + b_V) \cdot X + \text{constant} \\ m_{R,\text{inst}} &= m_{R,\text{Gaia-sp}} + c_R \\ &\quad + (k_{1,R} + a_R \cdot \text{UT} + b_R) \cdot X + \text{constant} \\ m_{I,\text{inst}} &= m_{I,\text{Gaia-sp}} + c_I \\ &\quad + (k_{1,I} + a_I \cdot \text{UT} + b_I) \cdot X + \text{constant} \end{aligned} \quad (8)$$

Here, in reality, Equation (7) is a polynomial. We start with the simplest case for our analysis. By fitting the data using this approach, we can obtain the coefficients. Subsequently, through a stepwise iteration, we can transform the monomials into a polynomial, thereby fully correcting the observed data.

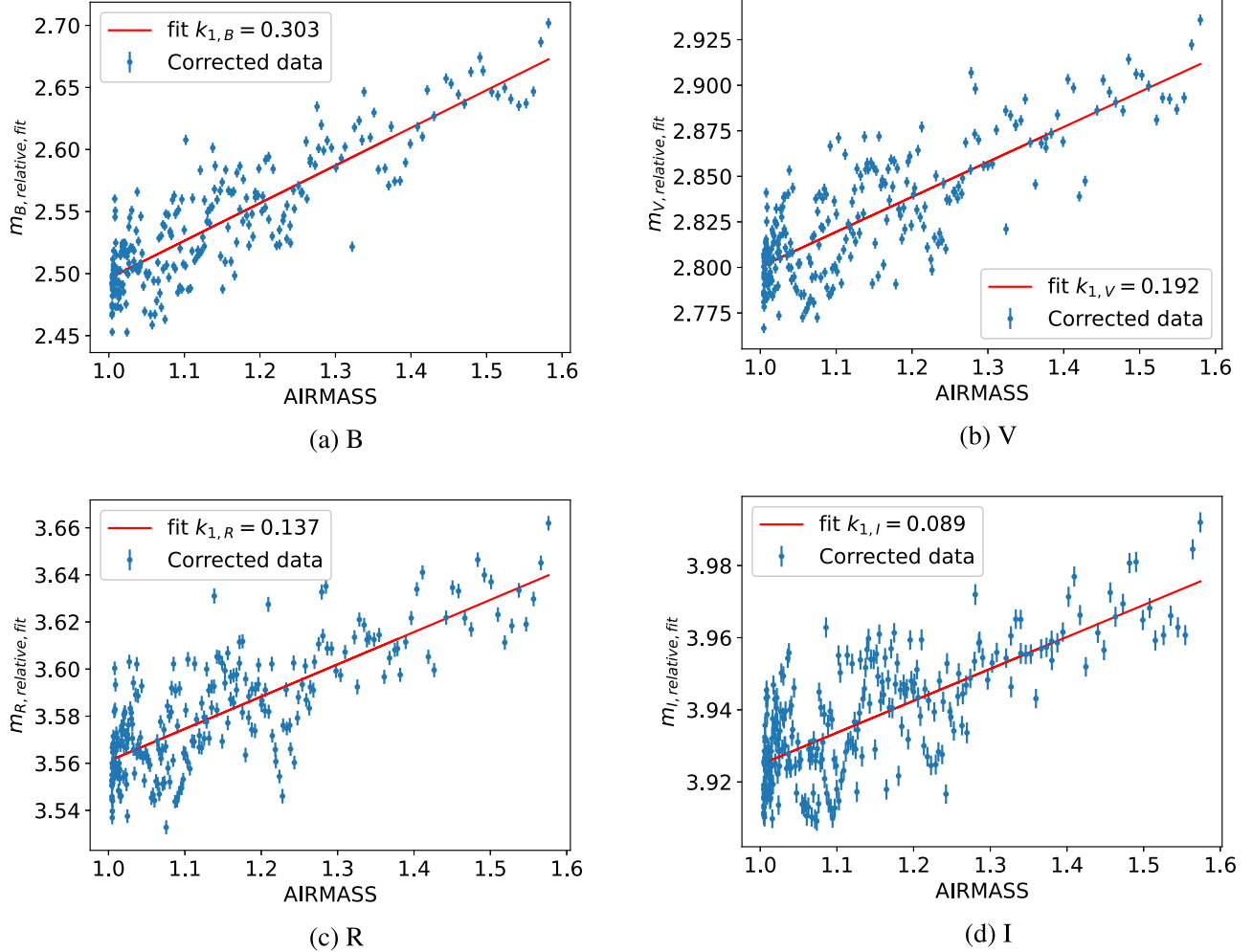


Figure 12. The corrected data and fitting results for SA 20-43 are presented. The x-axis represents airmass, while the y-axis means the difference between the instrumental magnitude and the Gaia-SP reference magnitude (m_{residual}). The blue dots represent the corrected data, while the red line delineates the linear fit obtained from the corrected data.

Table 13

The Results of the Four Bands on SA 20-43 are Obtained by Iterative Correction

Filter	k_1	σ_{k_1}	c_0	σ_{c_0}
B	0.303	0.013	2.192	0.036
V	0.192	0.012	2.622	0.032
R	0.137	0.009	3.245	0.024
I	0.089	0.006	3.826	0.028

This yields results shown in Figure 12, where the x-axis represents airmass and the y-axis means the difference between the instrumental magnitude and the Gaia-SP reference magnitude (m_{residual}). The blue dots represent the corrected data points, while the red line delineates the linear fit of the corrected data. The final results are summarized in Table 13. The coefficients k_1 and c_0 in Table 13 correspond to the

respective coefficients in Equation (8). σ_{k_1} and σ_{c_0} represent the simulated errors. $k_{1,B}$ is 0.303 ± 0.013 , $k_{1,V}$ is 0.192 ± 0.012 , $k_{1,R}$ is 0.137 ± 0.009 and $k_{1,I}$ is 0.089 ± 0.006 .

4.4.3. Comparison

Table 14 and Figure 13 compare all our measured extinction coefficients with those calculated for other telescopes at Xinglong Observatory (NAOC).

The results were nearly identical to others measured at Xinglong Observatory (NAOC).

4.5. Exoplanets

For exoplanets, we use differential photometry, which compares the light curves of stars within the field of view of an image, eliminating the influence of instruments and weather.

Table 14
Other Working Extinction Coefficients at Xinglong Observatory (NAOC)

Article	Telescope	Year	$k_{1,B}$	$k_{1,V}$	$k_{1,R}$	$k_{1,I}$
BD+39 3312 (this article)	60 cm	2023	0.335 ± 0.022	0.193 ± 0.018	0.090 ± 0.013	0.070 ± 0.017
SA 20-43 (this article)	60 cm	2022	0.303 ± 0.013	0.192 ± 0.012	0.137 ± 0.009	0.089 ± 0.006
Bai et al. (2018)	85 cm	2016	0.431 ± 0.029	0.282 ± 0.026	0.217 ± 0.019	0.156 ± 0.021
Huang et al. (2012)	80 cm	2011–2012	0.348 ± 0.022	0.236 ± 0.017	0.168 ± 0.019	0.085 ± 0.021
Huang et al. (2012)	80 cm	2006–2007	0.307 ± 0.009	0.214 ± 0.008	0.161 ± 0.008	0.091 ± 0.008
Huang et al. (2012)	80 cm	2004–2005	0.296 ± 0.012	0.199 ± 0.009	0.141 ± 0.010	0.083 ± 0.009
Zhou et al. (2009)	85 cm	2008	0.330 ± 0.007	0.242 ± 0.005	0.195 ± 0.004	0.066 ± 0.003
Shi et al. (1998)	60 cm	1998	0.31	0.22	0.14	0.10
Shi et al. (1998)	60 cm	1995	0.35	0.20	0.18	0.16

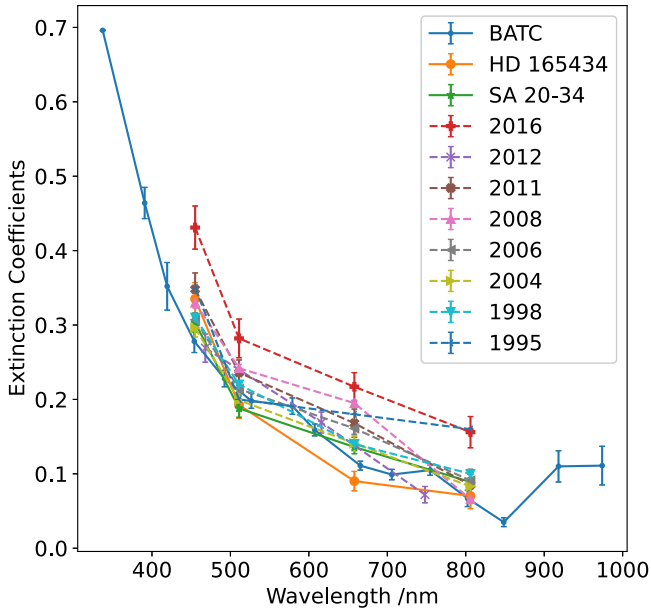


Figure 13. With other working extinction coefficients, the x -axis represents wavelength, while the y -axis means the extinction coefficient. The data labeled as BATC are sourced from Zhou et al. (2001), the data labeled 2012 are sourced from Zhao et al. (2020) and the data labeled 2011 are sourced from Huang et al. (2012).

The real used to correct the star, the reference star and the brightness of reference star cannot be too different from the target star, and the distance between the figure and the target cannot be too far. Additionally, the sigma of the light curve cannot be too large, i.e., 0.01, to ensure that it is not a variable star. The number of reference stars should be small, so that the image is the most appropriate. A comparable star, with the same requirements as the reference star, is also required at the end for final comparison.

4.5.1. HAT-P-32 b

For differential photometry, we can obtain its light curve. Figure 14 is the light curve extracted by us after differential

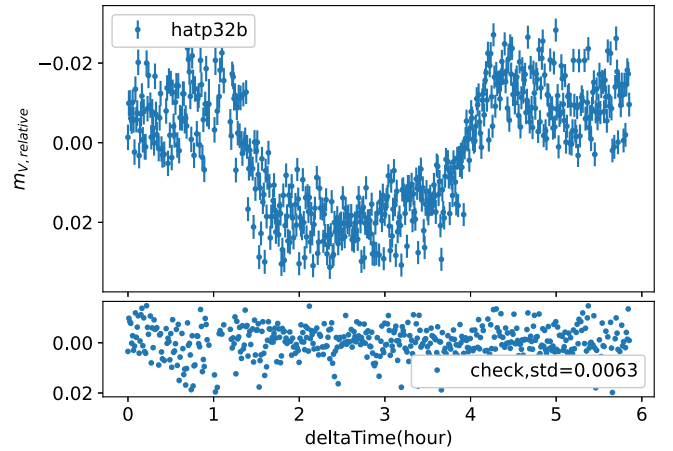


Figure 14. HAT-P-32 b original data. The upper panel shows the observed eclipse light curve of HAT-P-32 b, while the lower panel displays the photometric variation of the comparison stars. The same x -axis for both panels is deltaTime (hr), representing the time span from the beginning to the end of the observation. The y -axis of both panels represents the relative magnitude, $m_{V,relative}$.

correction. The top panel is the light curve of the host star of this exoplanet, and the bottom panel is the light curve of the reference star. The std in the label in the bottom panel stands for differential photometric accuracy, with scatter of 0.0063 mag. Then, we combine the five frames into one frame (binned 5) to increase the SNR in Figure 15(a). Figure 15(a) represents our photographic acquisition of HAT-P-32 b and its control star, and we can see the obvious eclipse light variation in the target, with scatter of which is 0.0037 mag. Figure 15(b) is the comparison of our light curve with those of other work from the literature, and they completely agree with each other, but the basic trend is clear. The data used in Figure 15(b) are described as follows. The observing equipment they used in the articles (Hartman et al. 2011; Nortmann et al. 2016) was the OSIRIS instrument of the Gran Telescopio CANARIAS (GTC) in long-slit spectral mode.

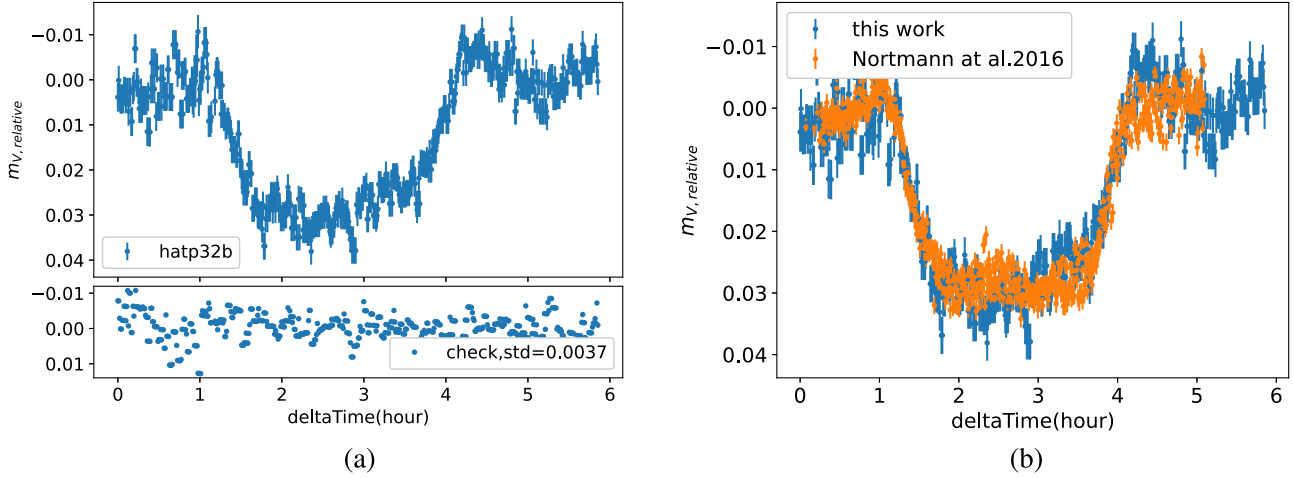


Figure 15. Comparison of HATP-32b light curve and HATP-32b light curve. (a) The eclipse light curve of HAT-P-32 b is shown in Figure 14, with data binned at a size of 5. (b) Comparison of eclipse light curves of HAT-P-32 b. Blue data points represent observations from this observation, i.e. the data in Fig. 1, and orange data points represent eclipse light curves from Nortmann et al. 2016.

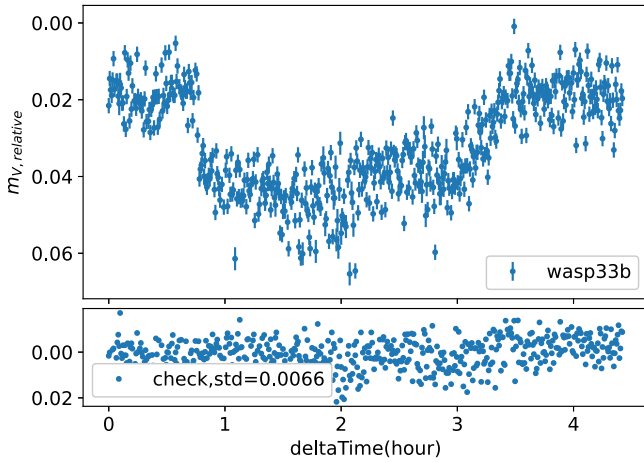


Figure 16. The upper panel shows the observed eclipse light curve of WASP-33 b, while the lower panel displays the variation of the comparison stars. The same x-axis for both panels is deltaTime (hr), representing the time span from the beginning to the end of the observation. The y-axis of both panels represents the relative magnitude, $m_{V,relative}$.

4.5.2. WASP-33 b

Since WASP-33 is a δ Scuti variable star (Herrero et al. 2011), this means that the light curve of the exoplanet contains the variation of the host star. The relationships in Figures 16 and 17(a) for WASP-33 b are the same as those in Figure 14, where the scatter is of 0.0066 mag, and Figure 15(a) for HAT-P-32 b, taken before and after binning 5. Figure 17(a) shows our light curve of WASP-33 b and its host star. We can even see its light variation of 0.02 mag clearly, while the precision of the former reference star is about 0.004 mag in the best situation. This depth of the evolutionary eclipse may include

the light variations of the host star. Comparing WASP-33 b with data obtained by other observers using CCD observations, our result also agrees well with Johnson et al. (2015) obtained from the 0.3 m telescope at Monte Carbre Observatory and the 0.8 m telescope at Montserrat Observatory in Figure 17(b).

We compare the observing performance of the 60 cm telescope using the CCD. From the articles Wang et al. (2017) and Wang et al. (2019), we see that they have 60 cm frames set up for exoplanets with differential photometric accuracy around 0.0016–0.0063 mag. The differential photometric accuracy obtained from our measurements is between 0.003 and 0.004 mag, which is comparable or even smaller than the references. Therefore, we conclude CMOS is suitable for observing exoplanets and can replace the CCD for this program.

5. Summary and Conclusions

In this work, the tests mainly include these items: Supersky flat field, the accuracy of photometry, the accuracy of differential photometry and the extinction coefficients with CMOS observations mounted on the 60 cm telescope at Xinglong Observatory (NAOC). Based on the tests, flat field correction for CMOS + 60 cm telescope could be better than 1% at *BVR* bands, and thus there is a change of flat field every day during the observation period. A flat field can be replaced by that of another day during our observations. Therefore, we conclude that the camera's performance is stable. The following are our conclusions: The open clusters result in a photometric accuracy of 0.02 mag. The calculated extinction coefficient of our work is compared with other coefficients observed at Xinglong Observatory (NAOC) using a standard

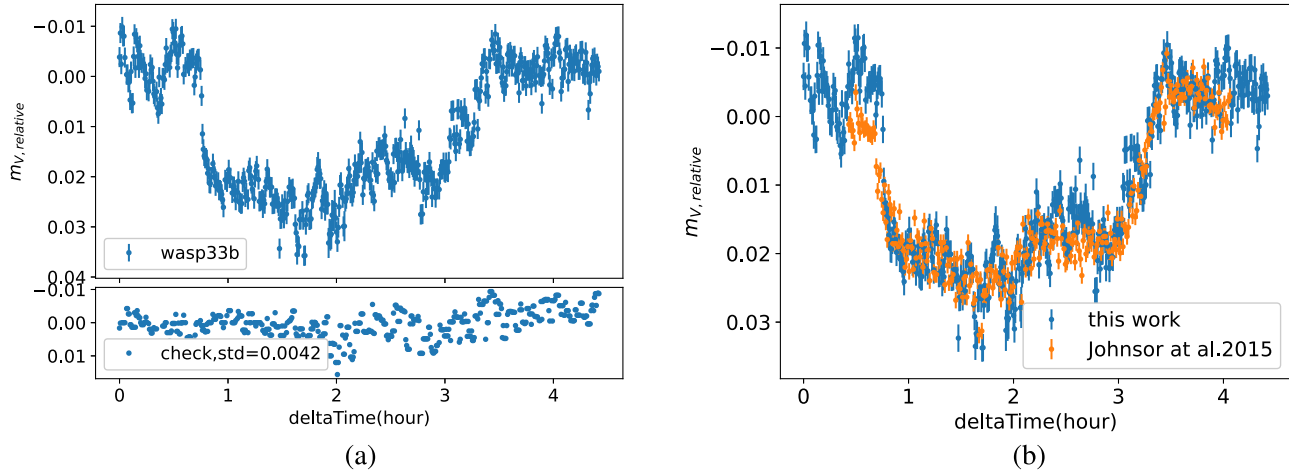


Figure 17. WASP-33 b light curve we collected and comparison of the different WASP-33 b light curves. (a) The eclipse light curve of WASP-33 b is shown in Figure 16, with data binned at a size of 5. (b) Comparison of eclipse light curves of WASP-33 b. Blue data points represent observations from this observation, i.e. the data in Fig. 1, and orange data points represent eclipse light curves from Johnson et al. 2015.

star, not revealing a significant difference. The differential photometric accuracy for exoplanets is 0.004 mag.

Therefore, we can conclude that the observation results of the observing system in this paper are in accordance with our expectations and can be used in scientific observations. This SONY IMX455 CMOS sensor satisfies our requirements and can replace the CCD.

In the future, we will test the pixel stability of this camera. We will also test it on other devices with exposure times of 60, 300, 600 and 1200 s. Additionally, we will study the dark current for each corresponding exposure time.

Acknowledgments

This work is supported by the Strategic Priority Research Program of the Chinese Academy of Sciences (grant Nos. XDB0550100, and XDB0550000), and supported by National Key R&D Program of China (grant No. 2023YFA1609700). We also acknowledge the National Natural Science Foundation of China (NSFC, Grant Nos. 12090041 and 12090040), and the science research grants from the China Manned Space Project with No. CMS-CSST-2021-B03. We also acknowledge the support of the staff at the Xinglong Observatory (NAOC).

References

- Abazajian, K. N., Adelman-McCarthy, J. K., Agüeros, M. A., et al. 2009, *APJS*, **182**, 5543
- Alarcon, M. R., Licandro, J., Serra-Ricart, M., et al. 2023, *PASP*, **135**, 055001
- Bai, C., Fu, J., Li, T., et al. 2018, *RAA*, **18**, 107
- Bertin, E., & Arnouts, S. 1996, *A&AS*, **117**, 393
- Bessell, M. S. 1990, *PASP*, **102**, 1181
- Bigas, M., Cabruja, E., Forest, J., & Salvi, J. 2006, *MJ*, **37**, 433–451
- Bonanno, G., Belluso, M., Cosentino, R., & Scuderi, S. 2003, *MEMSAI*, **74**, 800
- Boyle, W. S., & Smith, G. E. 1970, *BSTJ*, **49**, 587
- Calamida, A., Mack, J., Deustua, S., & Sabbi, E. 2018, Instrument Science Report *WFC3 2018-8*
- Cousins, A. W. J., & Caldwell, J. A. R. 2001, *MNRAS*, **323**, 380
- Fossum, E. R. 1997, *NIMPA*, **395**, 291
- Gaia Collaboration, Montegriffo, P., Bellazzini, M., et al. 2023, *A&A*, **674**, A33
- Gaia Collaboration, Vallenari, A., Brown, A. G. A., et al. 2023, *A&A*, **674**, A1
- Gallaway, M. 2016, An Introduction to Observational Astrophysics (Berlin: Springer), XVIII, 236
- Hartman, J. D., Bakos, G. Á, Torres, G., et al. 2011, *ApJ*, **742**, 59
- Herrero, E., Morales, J. C., Ribas, I., & Naves, R. 2011, *A&A*, **526**, L10
- Huang, B., Xiao, K., & Yuan, H. 2022, *SSPMA*, **52**, 289503
- Huang, F., Li, J.-Z., Wang, X.-F., et al. 2012, *RAA*, **12**, 1585
- Johnson, M. C., Cochran, W. D., Collier Cameron, A., & Bayliss, D. 2015, *ApJL*, **810**, L23
- Karpov, S., Bajat, A., Christov, A., Prouza, M., & Beskin, G. 2020, *Proc. SPIE*, **11454**, 114540G
- Kron, R. G. 1980, *ApJS*, **43**, 305
- Landolt, A. U. 2007a, in ASP Conf. Ser., 364, The Future of Photometric, Spectrophotometric and Polarimetric Standardization, ed. C. Sterken (San Francisco, CA: ASP), 27
- Landolt, A. U. 2007b, *AJ*, **133**, 2502
- Landolt, A. U. 2013, *AJ*, **146**, 131
- Law, N. M., Corbett, H., Galliher, N. W., et al. 2022, *PASP*, **134**, 035003
- Li, D., Shang, Y.-Y., & Song, Q. 2006, *PNAOC*, **3**, 380
- Licandro, J., Tonry, J., Alarcon, M. R., Serra-Ricart, M., & Denneau, L. 2023, *LPICo*, **2851**, 2262
- Munari, U., Henden, A., Frigo, A., et al. 2014, *AJ*, **148**, 81
- Northmann, L., Pallé, E., Murgas, F., et al. 2016, *A&A*, **594**, A65
- Ofek, E. O., Ben-Ami, S., Polishook, D., et al. 2023, *PASP*, **135**, 065
- Oke, J. B., & Gunn, J. E. 1983, *APJ*, **266**, 713
- Qiu, P., Zhao, Y., Zheng, J., Wang, J.-F., & Jiang, X.-J. 2021, *RAA*, **21**, 268
- Shi, H.-M., Qiao, Q.-Y., Hu, J.-Y., & Lin, Q. 1998, *ChA&A*, **22**, 245
- Tonry, J. L., Denneau, L., Heinze, A. N., et al. 2018, *PASP*, **130**, 064505
- Wang, Y.-H., Wang, S., Hinse, T. C., et al. 2019, *AJ*, **157**, 82
- Wang, Y.-H., Wang, S., Liu, H.-G., et al. 2017, *AJ*, **154**, 49
- Yan, H., Burstein, D., Fan, X. H., et al. 2000, *PASP*, **112**, 691
- Yang, H., Haibo, Y., Chengyuan, L., et al. 2021, *APJ*, **907**, 68
- Zhao, Y., Fan, Z., Ge, L., et al. 2020, *Ap&SS*, **365**, 11
- Zhou, A.-Y., Jiang, X.-J., Zhang, Y.-P., & Wei, J.-Y. 2009, *RAA*, **9**, 349
- Zhou, X., Jiang, Z.-J., Xue, S.-J., et al. 2001, *ChJAA*, **1**, 372